

## Structure evolution and dielectric behavior of polystyrene-capped barium titanate nanoparticles

H. Z. Guo,<sup>a</sup> Ya. Mudryk,<sup>b</sup> M. I. Ahmad,<sup>a</sup> X. C. Pang,<sup>ac</sup> L. Zhao,<sup>ac</sup> M. Akinc,<sup>a</sup> V. K. Pecharsky,<sup>ab</sup> N. Bowler,<sup>a</sup> Z. Q. Lin<sup>ac</sup> and X. Tan<sup>\*a</sup>

Received 17th August 2012, Accepted 20th September 2012

DOI: 10.1039/c2jm35600g

Polystyrene-capped barium titanate (BaTiO<sub>3</sub>) nanoparticles with sizes of 11 nm and 27 nm were prepared using amphiphilic star-like diblock copolymer templates. The crystal structure evolution of these nanoparticles over a wide temperature range (10–428 K) was investigated by powder X-ray diffraction. The Rietveld refinement indicates that the abrupt structural transitions observed in micron-sized powders become broad as the particle size is reduced to a few tens of nanometers. The orthorhombic phase (*Amm2*) is observed in the range of 10–388 K, coexisting with the rhombohedral phase (*R3c*) at lower temperatures and with the tetragonal phase (*P4mm*) at higher temperatures. At room temperature (300 K), polystyrene-capped BaTiO<sub>3</sub> nanoparticles, both 11 and 27 nm sizes, primarily adopt the tetragonal phase, transforming to the cubic phase (*Pm3m*) at 398 K during heating. The phase evolution of the nanoparticles correlates well with their dielectric behavior. With the Landauer–Bruggeman effective approximation, the dielectric properties at room temperature of the BaTiO<sub>3</sub> core were calculated and the results are in agreement with the size effect of BaTiO<sub>3</sub> nanocrystals.

## 1. Introduction

Barium titanate (BaTiO<sub>3</sub>), one of the most commonly used perovskite compounds for electrical devices, has been extensively studied with focus on its crystallographic transitions and dielectric/ferroelectric behaviors.<sup>1</sup> A bulk BaTiO<sub>3</sub> crystal is in the paraelectric cubic phase with the *Pm3m* symmetry above the Curie temperature ( $T_C$ ) of 403 K and becomes ferroelectric through a sharp displacive phase transition to the tetragonal *P4mm* phase. The ferroelectric BaTiO<sub>3</sub> crystal undergoes two further structural transitions to orthorhombic *Amm2* at 273 K ( $T_{OT}$ ) and rhombohedral *R3m* at 183 K ( $T_{RO}$ ).<sup>2</sup>

A long-standing issue of interest concerning BaTiO<sub>3</sub> and other ferroelectric crystals is the so-called ‘size effect’, *i.e.* the size-dependence of their dielectric/ferroelectric properties and structural transitions.<sup>3–5</sup> This issue is now particularly prominent and technologically relevant because the length scale of these crystals is in the nanometer range when they are applied in miniaturized electronic devices. Many theoretical and experimental studies<sup>6–15</sup> have been conducted on BaTiO<sub>3</sub> in order to identify the critical size below which BaTiO<sub>3</sub> retains its cubic paraelectric structure at room temperature, yet there is still no consensus on this issue.

Based on the X-ray diffraction experiments at several temperatures, Uchino *et al.*<sup>7</sup> reported a critical size of 120 nm at which the  $T_C$  gradually lowered, and the cubic paraelectric phase became stable at room temperature. Aoyagi *et al.*<sup>8</sup> reported similar findings with the critical size of approximately 100 nm. However, these results are not in agreement with other reports where the critical size was estimated to be on the order of 10–20 nm.<sup>16–18</sup> Using the phenomenological Landau–Devonshire theory, Wang *et al.* calculated the critical size to be 44 nm.<sup>10</sup> This value is close to the experimental results of Hoshina and Wada *et al.*,<sup>11–13</sup> where a critical size of 30 nm was found. However, the  $T_C$  remains constant at 408 K for larger particles and the expected lowering of  $T_C$  when the particle size approaches 30 nm was not observed.

The particle size not only influences the Curie temperature,  $T_C$ , at which the paraelectric cubic and ferroelectric tetragonal transition occurs, but also impacts the ferroelectric transitions at  $T_{OT}$  and  $T_{RO}$ . Again, the reports in the literature are inconsistent. An X-ray diffraction study<sup>8</sup> indicates that  $T_{OT}$  shifts from 285 K down to 260–270 K when the particle size decreases to 100 nm while a low-temperature heat-capacity measurement on 100 nm particles shows that  $T_{RO}$  does not display any anomaly.<sup>9</sup> However, these observations seem to contradict a differential scanning calorimetry investigation where an increase of  $T_{OT}$  was noticed with decreasing grain size.<sup>6</sup> Hoshina and Wada *et al.*<sup>11–13</sup> found that, for BaTiO<sub>3</sub> particles larger than the critical size of 30 nm,  $T_{OT}$  was independent of the particle size while  $T_{RO}$  moves to higher temperatures with decreasing particle size. In contrast,

<sup>a</sup>Department of Materials Science and Engineering, Iowa State University, Ames, Iowa 50011, USA. E-mail: xtan@iastate.edu

<sup>b</sup>The Ames Laboratory of US Department of Energy, Iowa State University, Ames, Iowa 50011, USA

<sup>c</sup>School of Materials Science and Engineering, Georgia Institute of Technology, Atlanta, GA 30332, USA

several studies suggested an increase in  $T_{RO}$  and  $T_{OT}$ , and a decrease in  $T_C$  with the decreasing crystal size.<sup>6,7,14,15</sup>

Most previous studies on the size effect in  $BaTiO_3$  were focused on nominally bare particles, polycrystalline ceramics or even  $BaTiO_3$ -polymer composites.<sup>19–24</sup> And the dielectric characterization of the  $BaTiO_3$ -polymer composites in the literature is limited to the volume fraction dependence of the room temperature permittivity.<sup>20,25,26</sup> Polymer-capped  $BaTiO_3$  nanoparticles have rarely been synthesized, and the size effect on their dielectric properties is seldom presented. In the present work, two sizes of polystyrene-capped  $BaTiO_3$  (PS-BTO) nanoparticles, with  $BaTiO_3$  core of 11 nm (PS-BTO11) and 27 nm (PS-BTO27) diameter, were synthesized by chemical routes and their structure evolution was examined by powder X-ray diffraction. With the PS capping, the nanoparticles were hot-pressed into fully dense nanocomposite specimens (without growth of the original  $BaTiO_3$  core) and their dielectric behaviors were evaluated. By comparing their structure and properties, the particle size effect is clearly revealed.

## 2. Experimental

### 2.1 Synthesis

First, four amphiphilic 21-arm, star-like poly(acrylic acid)-*b*-polystyrene (PAA-*b*-PS) diblock copolymers with precisely tailorable molecular architectures, different molecular weights, and varied PAA to PS block ratios were synthesized by sequential atom transfer radical polymerization according to a previously described procedure.<sup>27</sup> Ferroelectric  $BaTiO_3$  nanoparticles were then synthesized *via* a wet chemistry approach by interacting nanoparticle precursors with the inner PAA block of the star-like PAA-*b*-PS diblock copolymer. In a typical process, a certain amount of the star-like PAA-*b*-PS (the molecular weights of each PAA and PS arm are 8.4k, and 5.2k, respectively) template was dissolved in *N,N*-dimethylformamide (DMF) at room temperature to form unimolecular micelles, followed by the addition of the appropriate amount of precursors (*i.e.*,  $BaCl_2 \cdot 2H_2O + TiCl_4 + NaOH$ ) that can be selectively incorporated into the inner PAA core through the coordination bonding between the acetic acid group in the PAA block and the metal ions of precursors. These  $BaTiO_3$  precursors are not expected to interact with the outer PS shell as the PS block does not have any active functional groups to coordinate with the precursors. The solution was then refluxed at 180 °C under argon for 2 hours, yielding ferroelectric  $BaTiO_3$  nanoparticles (diameter = 11 nm) capped with hydrophobic PS. PS-capped  $BaTiO_3$  nanoparticles with a diameter of 27 nm were also prepared by using the same approach with different molecular weights of diblock copolymer arms (the molecular weights of each PAA and PS arm are 28.1k and 29.7k, respectively). The size and morphology of PS-capped  $BaTiO_3$  nanoparticles were characterized by transmission electron microscopy (JEOL 1200EX STEM). The volume fraction of  $BaTiO_3$  nanoparticles in the PS-BTO nanocomposites was determined by thermogravimetric analysis (TGA).

For comparison, micron-sized  $BaTiO_3$  powder was also prepared *via* the solid-state reaction approach by reacting stoichiometric amounts of  $TiO_2$  (purity 99.99 wt%) and  $BaCO_3$  (purity 99.9 wt%) at 1373 K for 6 h.

### 2.2 Low temperature powder X-ray diffraction

The PS-BTO nanoparticles and micron-sized  $BaTiO_3$  particles were mixed with GE varnish in a copper sample holder. After curing, the samples were polished using 400 grit sandpaper in order to produce the flat surface required for the Bragg-Brentano powder diffraction geometry. The isothermal X-ray powder diffraction measurements were carried out at different temperatures ranging between 320 and 5 K during cooling on a Rigaku TTRAX rotating anode powder diffractometer employing Mo  $K\alpha$  radiation. The diffractometer is equipped with a continuous flow  $^4He$  cryostat that controls the sample temperature.<sup>28</sup> The scattered intensity was recorded as a function of Bragg angle ( $2\theta$ ) using a scintillation detector with a step of  $0.01^\circ 2\theta$ . The maximum intensity to lowest background intensity ratio was close to 350 with the strongest Bragg peaks registering nearly 7000 counts at their peak values, which corresponds to  $\sim 1.2\%$  statistical spread. The range of measured Bragg angles was from  $8^\circ$  to  $56^\circ 2\theta$ . The program LHPM Rietica<sup>29</sup> was employed to carry out the full-profile Rietveld refinement of every recorded pattern. The significant peak overlapping occurring due to crystallographic similarities of different polymorphic modifications of  $BaTiO_3$  complicated the quantitative phase analysis of these phases, especially in the PS-BTO11 and PS-BTO27 samples. Several assumptions were made during the refinement, including (1) the atomic coordinates were fixed to be the same in the corresponding crystal structures for both micron-sized and nano-sized powders; (2) the profile parameters used in the Rietveld refinement were the same for all crystallographic polymorphs in the entire temperature range studied, for a given particle size; (3) the isotropic thermal displacement parameters of all atoms in each phase were assumed to be the same at a given temperature employing, in effect, the overall isotropic thermal displacement approximation; (4) the rhombohedral angle of the low temperature structure of nano-sized samples was fixed to the value obtained during the refinement of the micron-sized powder. These assumptions did not, however, degrade the quality of the refinement as can be seen from the values of the profile residuals,  $R_p \sim 0.09$ , and the derived Bragg residuals,  $R_{Bragg} \sim 0.02$  to  $0.04$ .

### 2.3 High temperature powder X-ray diffraction

The high temperature X-ray powder diffraction measurements were carried out on a PANalytical X'Pert PRO diffractometer equipped with a temperature controlled hot stage using Cu  $K\alpha$  radiation. The loose "as prepared" powders (not mixed with varnish or sintered) were used in this experiment. The diffraction data were collected at constant temperatures during heating, at 10 K intervals, from 298 K to 428 K. At each temperature, the scattered intensity was recorded as a function of Bragg angle ( $2\theta$ ) using an X'Celerator detector with a step size of  $0.0167^\circ$  in the  $2\theta$  range from  $10^\circ$  to  $120^\circ$ . The collection time at each step was 120 s. Pure silica (hexagonal form) was used as an internal standard. The increase in the height of the sample stage arising from expansion of the alumina support rod was compensated for using a step motor. General Structural Analysis System (GSAS)<sup>30</sup> software was employed to carry out the full-profile Rietveld refinement of every recorded pattern. Scale factor, lattice

parameters, background (6 order shifted Chebyshev polynomial approximation), and pseudo-Voigt profile function (only Lorentzian crystalline broadening coefficient LX and Gaussian instrument response coefficient GW) parameters were refined initially. In the later stages of the refinements, atomic parameters of heavy elements Ti and Ba were also refined. The profile residuals,  $R_p$ , were less than 0.09, and the derived Bragg residuals,  $R_{\text{Bragg}}$ , were between  $\sim 0.04$  and  $\sim 0.07$ .

## 2.4 Dielectric characterization

Disk-shaped samples for dielectric measurements, with diameter approximately 12.5 mm and thickness approximately 1 mm, were prepared using a hot press. PS-BTO powders were heated to 443 K and die-pressed at 21 MPa for 5 minutes. A thin film of silver was then sputtered on both flat surfaces as electrodes. Dielectric constant and loss tangent under the weak electric field were measured at 1, 10, and 100 kHz with an LCZ meter (KEITHLEY 3330) in conjunction with a temperature chamber. Measurements below room temperature were carried out during continuous cooling with liquid  $\text{N}_2$  to 113 K at a rate of  $3 \text{ K min}^{-1}$  while those above room temperature were performed during continuous heating to 433 K at the same rate. As a reference, dielectric measurements were also made on a pure PS sample with a Novocontrol dielectric spectrometer at constant temperatures during heating at 10 K intervals between 233 K and 403 K.

## 3. Results and discussion

Transmission electron microscopy was used to examine the particle size and morphology of PS-BTO nanoparticles. As shown in Fig. 1, all particles were nearly spherical in shape. According to image analysis, the particle sizes are  $11 \pm 1.2 \text{ nm}$  (Fig. 1a) and  $27 \pm 2.1 \text{ nm}$  (Fig. 1b), respectively. The higher magnification micrographs shown as insets in Fig. 1 indicate that an amorphous oxide surface layer might be present on the nanoparticles, especially PS-BTO11. The existence of the PS capping layer on these  $\text{BaTiO}_3$  nanoparticles was confirmed by the easy dispersion of  $\text{BaTiO}_3$  nanoparticles in the toluene solvent and other tests. The weight fraction of PS in these PS-BTO nanoparticles was measured to be 13.92% (PS-BTO11) and 15.48% (PS-BTO27) from TGA experiments, as shown in Fig. 2. Based on the mass density of PS ( $1.05 \text{ g cm}^{-3}$ ) and  $\text{BaTiO}_3$  ( $6.02 \text{ g cm}^{-3}$ ), the volume fractions of the inorganic  $\text{BaTiO}_3$  core calculated from the mass loss from TGA tests are 51.9% and 48.8%, respectively.

The profiles of the pseudo-cubic  $(111)_c$  and  $(200)_c$  Bragg peaks of the PS-BTO nanoparticles at selected temperatures are displayed in Fig. 3, with those from the micron-sized  $\text{BaTiO}_3$  particles shown in Fig. 3e as a reference. Except the profiles at 420 K indicating a single cubic phase, all other peak profiles in Fig. 3 for both PS-BTO11 and PS-BTO27 have to be fitted with two or three Bragg peaks representing coexisting polymorphic phases of  $\text{BaTiO}_3$ . The Rietveld refinement at low temperatures was performed assuming a two-phase mixture, either orthorhombic–rhombohedral or orthorhombic–tetragonal. There is a clear difference between the Bragg peak profiles of the PS-BTO nanoparticles and the micron-sized  $\text{BaTiO}_3$ . Presumably the PS capping on the nanoparticles does not contribute to the Bragg

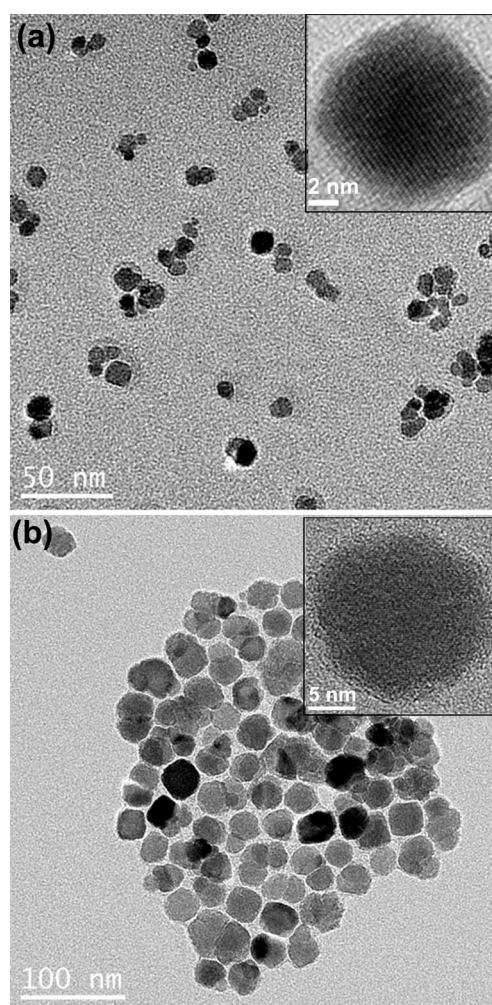


**Fig. 1** Transmission electron microscopy micrographs of polystyrene capped  $\text{BaTiO}_3$  nanoparticles with sizes of (a) 11 nm and (b) 27 nm. The insets show the higher magnification images.

intensity, and the difference cannot be explained by strain-size broadening of the Bragg peaks alone. The X-ray diffraction patterns of micron-sized  $\text{BaTiO}_3$  particles (only a small  $2\theta$  region is shown for clarity) indicate a single phase at each temperature

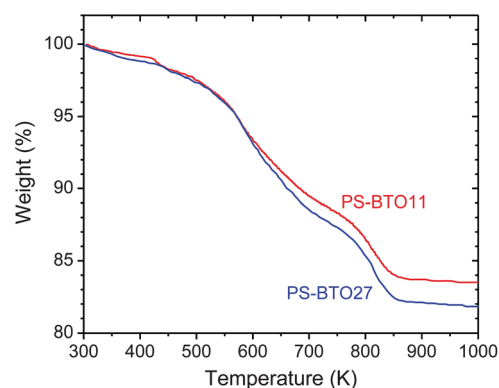


**Fig. 2** The thermogravimetric analysis of the PS-capped  $\text{BaTiO}_3$  nanoparticles.

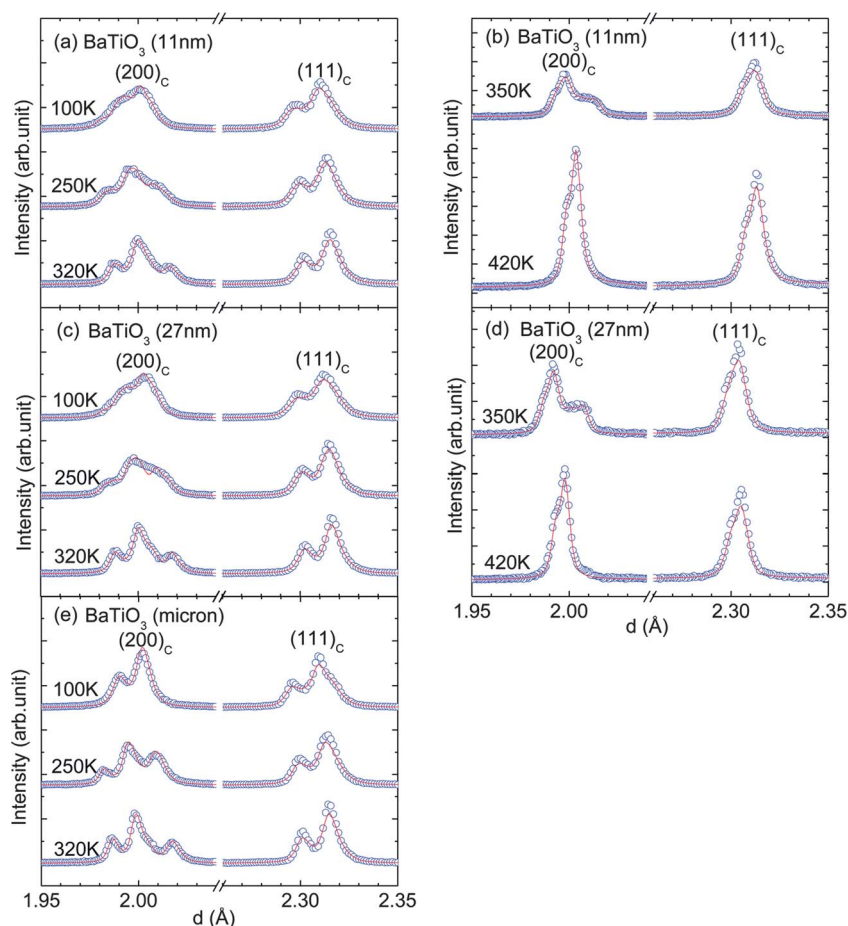


**Fig. 3** X-ray diffraction peak profiles at selected temperatures for the pseudo-cubic  $(200)_c$  and  $(111)_c$  Bragg peaks from (a) PS-BTO11 at low temperatures, (b) PS-BTO11 at high temperatures, (c) PS-BTO27 at low temperatures, (d) PS-BTO27 at high temperatures, and (e) micron-sized  $\text{BaTiO}_3$  powder at low temperatures.

shown in Fig. 3e, which is consistent with the typical phase transition sequence of conventional (not nanosized)  $\text{BaTiO}_3$  materials. Both PS-BTO11 and PS-BTO27 nanoparticles display a similar  $(111)_c$  peak splitting but a more diffuse  $(200)_c$  peak when compared with the micron-sized  $\text{BaTiO}_3$  powder.

The volume fraction of each phase as a function of temperature in PS-BTO11 and PS-BTO27, as well as that in the micron-sized  $\text{BaTiO}_3$ , is plotted in Fig. 4. It is easy to notice a slight difference ( $\sim 15\%$ ) between phase compositions near room temperature determined by high-temperature vs. low-temperature X-ray diffraction methods. Such discrepancy can be explained by (a) a different particle environment (loose powder vs. embedded in varnish); (b) the difference in the instrument resolution (resolution is higher for the low temperature data); and (c) the difference in absorption of X-rays by both the  $\text{BaTiO}_3$  cores and polymer caps (low energy  $\text{Cu K}\alpha$  radiation is absorbed to a much greater degree compared with the high energy  $\text{Mo K}\alpha$  radiation). Nevertheless, there is a clear qualitative agreement between the high-temperature and low-temperature X-ray powder diffraction data indicative of a coexistence of tetragonal (main) and orthorhombic (minority) phases at room temperature in the nanoparticles.

The low-temperature experiment performed for the micron-sized  $\text{BaTiO}_3$  powder shows two mixed-phase regions: the

coexistence of rhombohedral and orthorhombic phases between 160 K and 200 K; orthorhombic and tetragonal phases between 260 K and 310 K. At other temperatures, single phases are observed. In the PS-BTO11 and PS-BTO27 nanoparticles containing  $\sim 80\%$  of the tetragonal phase and  $\sim 20\%$  of the orthorhombic phase at room temperature, the tetragonal phase gradually transforms to the orthorhombic phase during cooling to low temperatures. The amount of the orthorhombic phase reaches a peak value of  $\sim 70\%$  at  $\sim 210$  K. A further decrease in temperature leads to a gradual formation of the rhombohedral phase, reaching the maximum  $\sim 80\%$  at 10 K. During the warming-up of these PS-BTO nanoparticles from 308 K to 428 K, the volume fraction of the coexisting orthorhombic and tetragonal phases stays more or less the same up to 388 K. At 398 K, the orthorhombic phase disappears and both PS-BTO11 and PS-BTO27 become a mixture of the tetragonal and cubic phases with the cubic one dominant. The PS-BTO11 becomes a single cubic phase at 428 K while the PS-BTO27 becomes a single cubic phase at 408 K.

It is also noted that the level of the lattice distortion is directly related to the particle size. The lattice parameters of the major phase at different temperatures are listed in Table 1 for both PS-BTO11 and PS-BTO27, as well as the micron-sized  $\text{BaTiO}_3$  powder. Using the tetragonal phase at 320 K as an example, the

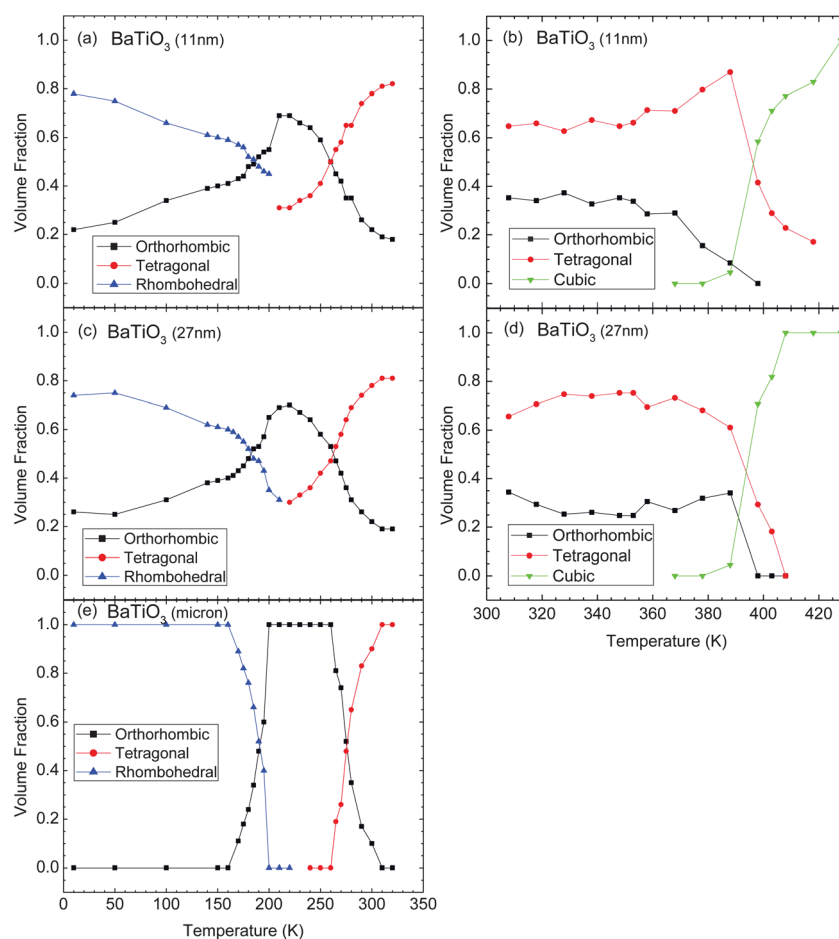


**Fig. 4** Temperature dependence of the volume fraction of the various phases in (a) PS-BTO11 at low temperatures, (b) PS-BTO11 at high temperatures, (c) PS-BTO27 at low temperatures, (d) PS-BTO27 at high temperatures, and (e) micron-sized BaTiO<sub>3</sub> powder at low temperatures.

*cla* ratio of the tetragonal lattice decreases from 1.0094 for the micron-sized powder to 1.0088 for PS-BTO27, and 1.0084 for PS-BTO11. For the orthorhombic lattice the *b* and *c* lattice parameters become closer in PS-BTO nanoparticles as compared to the micron-sized powder.

It should be noted that although the two-phase coexistence, either orthorhombic–rhombohedral or orthorhombic–tetragonal, was assumed at low temperatures for the Rietveld refinement, it remains possible that three phases, *i.e.* orthorhombic, rhombohedral, and tetragonal, may coexist in a limited temperature range around 210 K. This is similar to the coexistence of orthorhombic, tetragonal and cubic phases at

temperatures around 400 K. However, this does not necessarily mean that all of the phases coexist in individual nanoparticles. It is also possible that some of the individual nanoparticles are single phase. Due to size and chemistry variation,<sup>31</sup> some are in the orthorhombic phase while others are in the tetragonal phase at room temperature.

The temperature dependent dielectric properties of PS-BTO11 and PS-BTO27 were measured on hot-pressed dense nanocomposite disks. As shown in Fig. 5, data below room temperature were taken during cooling while those above room temperature were recorded during heating in order to be consistent with the X-ray powder diffraction experiments. For

**Table 1** Lattice parameters for the major phases of BaTiO<sub>3</sub> particles at selected temperatures

Temperature (K)	Symmetry	BaTiO <sub>3</sub> (11 nm)	BaTiO <sub>3</sub> (27 nm)	BaTiO <sub>3</sub> (micron)
100	<i>R3m</i>	<i>a</i> = 4.0056(1) <i>α</i> = 89.87°	<i>a</i> = 4.0063(1) <i>α</i> = 89.87°	<i>a</i> = 4.0069(1) <i>α</i> = 89.86°
250	<i>Amm2</i>	<i>a</i> = 3.9915(1) <i>b</i> = 5.6888(4) <i>c</i> = 5.6777(3)	<i>a</i> = 3.9904(2) <i>b</i> = 5.6869(4) <i>c</i> = 5.6969(6)	<i>a</i> = 3.9910(1) <i>b</i> = 5.6798(2) <i>c</i> = 5.6914(3)
320	<i>P4mm</i>	<i>a</i> = 4.0014(1) <i>c</i> = 4.0350(1)	<i>a</i> = 4.0012(1) <i>c</i> = 4.0364(1)	<i>a</i> = 3.9998(1) <i>c</i> = 4.0373(1)
420	<i>Pm3̄m</i>	<i>a</i> = 4.0112(1)	<i>a</i> = 4.0113(1)	

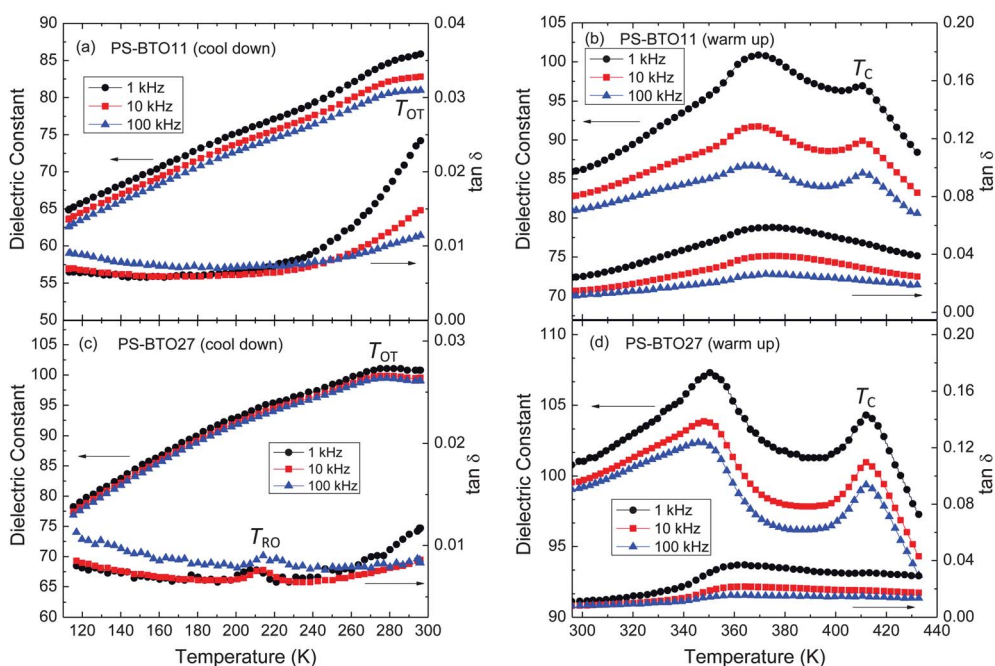


**Fig. 5** Temperature dependence of dielectric properties of (a) PS-BTO11 during cooling, (b) PS-BTO11 during heating, (c) PS-BTO27 during cooling, and (d) PS-BTO27 during heating.

the PS-BTO11, the dielectric constant shows a monotonic decrease during cooling from room temperature to 113 K. In this range, there is only one noticeable anomaly at  $\sim 283$  K (Fig. 5a) which may correspond to the fast increase of the orthorhombic phase volume fraction ( $T_{OT}$ ). During heating of the PS-BTO11 sample, an obvious frequency dispersion in the dielectric properties is seen, and two peaks can be found at  $\sim 363$  K and  $\sim 413$  K on the dielectric constant curves (Fig. 5b). The peak at  $\sim 413$  K is apparently related to the abrupt formation of the cubic phase ( $T_C$ ). The PS-BTO27 sample displays a higher dielectric constant with weaker frequency dispersion. In addition, the dielectric anomalies become more apparent during the cooling process; one at  $\sim 273$  K on the dielectric constant curves and the other at  $\sim 210$  K on the loss tangent curves (Fig. 5c). Apparently, the anomaly at  $\sim 273$  K is associated with the formation of the orthorhombic phase ( $T_{OT}$ ) while the other one is related to the formation of the rhombohedral phase ( $T_{RO}$ ). The dielectric anomalies also become more prominent during heating in PS-BTO27 than in PS-BTO11, with one at  $\sim 353$  K and the other at  $\sim 413$  K (Fig. 5d). Again, the dielectric peak at  $\sim 413$  K originates from the formation of the cubic paraelectric phase ( $T_C$ ).<sup>2</sup> Compared with the sharp transitions in conventional BaTiO<sub>3</sub> ceramic powders,<sup>2</sup> transitions in PS-capped BaTiO<sub>3</sub> nanoparticles are broadened and smeared. Especially in PS-BTO11, the transition at  $T_{RO}$  becomes invisible and that at  $T_{OT}$  is hardly seen from dielectric measurements. This can be attributed to the size distribution of nanoparticles, the persistence of the orthorhombic phase throughout the temperature range due to an incomplete structural transition, and the dilution effect from non-ferroelectric PS. In addition, it appears that all transition temperatures,  $T_{RO}$  ( $\sim 210$  K for PS-BTO27),  $T_{OT}$  ( $\sim 283$  K for PS-BTO11 and  $\sim 273$  K for PS-BTO27), and  $T_C$  ( $\sim 413$  K for both PS-BTO11 and PS-BTO27), are shifted to

higher temperatures in these PS-capped nanoparticles compared to micron sized BaTiO<sub>3</sub> ( $T_{RO} = 183$  K,  $T_{OT} = 273$  K, and  $T_C = 403$  K).<sup>2</sup>

It should be pointed out that an extremely high dielectric constant (85–100 at 1 kHz at room temperature) was measured from the present PS-capped BaTiO<sub>3</sub> nanocomposites. This value is usually below 50 under the same measuring conditions in previous studies on other BaTiO<sub>3</sub>-polymer nanocomposites.<sup>23,26,32</sup> The ultrahigh dielectric constant observed in the present work can be attributed to the fact that the BaTiO<sub>3</sub> core is still ferroelectric in both PS-capped nanoparticles. The ferroelectric phase of BaTiO<sub>3</sub> generally has a higher dielectric constant than the cubic paraelectric phase.<sup>33</sup> Another contributing factor is the high volume fraction and uniform dispersion

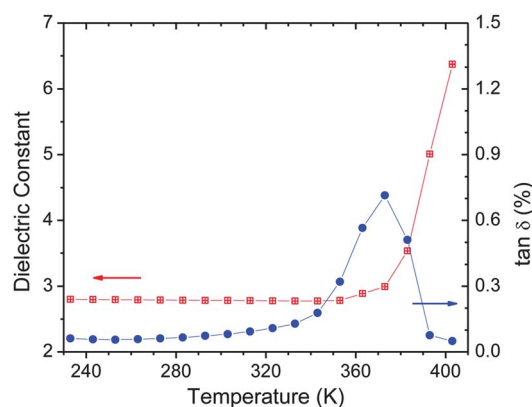


**Fig. 6** Temperature dependence of dielectric properties of pure polystyrene measured at 1 kHz at selected temperatures with 10 K intervals during heating.

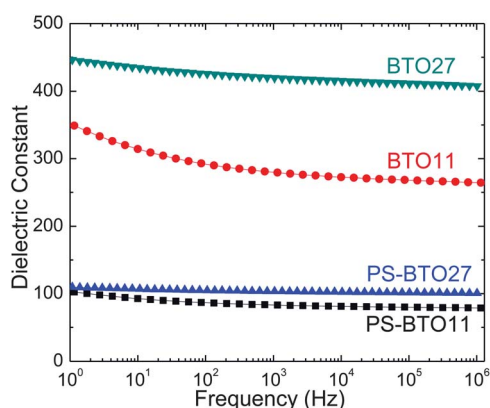


**Fig. 7** The frequency dependence of dielectric constant at room temperature of PS-BTO11 and PS-BTO27 and the calculated dielectric constant of the BaTiO<sub>3</sub> cores. BTO11 denotes the 11 nm core while BTO27 denotes the 27 nm core.

of the BaTiO<sub>3</sub> nanoparticles in the PS matrix. In the present work, the nanocomposites were produced by hot-pressing of BaTiO<sub>3</sub> nanoparticles that were individually coated with PS. The volume fractions of the ferroelectric BaTiO<sub>3</sub> are high in both composites (51.9% and 48.8%, respectively).

In Fig. 5, the dielectric anomalies at ~363 K in PS-BTO11 and at ~353 K in PS-BTO27 do not correspond to any structural changes in the BaTiO<sub>3</sub> core. Our differential scanning calorimetry measurements on pure PS with the same molecular weight as those capping the BaTiO<sub>3</sub> nanoparticles indicate that PS undergoes glass transition in this temperature range. Furthermore, dielectric properties measured at discrete temperatures with 10 K intervals on pure PS, Fig. 6, confirm the presence of a dielectric anomaly at the glass transition temperature ( $T_g$ ).

The PS-BTO samples for dielectric measurements can be considered as a composite of two phases: PS as the matrix and the BaTiO<sub>3</sub> nanoparticles as the inclusion. Various models have been used for the evaluation of the dielectric constant of two phase composites.<sup>34–36</sup> With these models, the effective dielectric constant of the BaTiO<sub>3</sub> core can be extracted from the data obtained from the dielectric measurements of PS-BTO nanocomposites. Considering the high volume fraction of the BaTiO<sub>3</sub> nanoparticles, the Landauer–Bruggeman effective approximation<sup>35,36</sup> is appropriate for the calculation. The mathematical expression of the approximation is

$$\gamma \frac{\epsilon_1 - \epsilon_{\text{eff}}}{\epsilon_1 + 2\epsilon_{\text{eff}}} + (1 - \gamma) \frac{\epsilon_2 - \epsilon_{\text{eff}}}{\epsilon_2 + 2\epsilon_{\text{eff}}} = 0 \quad (1)$$

where  $\gamma$  denotes the volume fraction of the inclusion, and  $\epsilon_{\text{eff}}$ ,  $\epsilon_1$  and  $\epsilon_2$  stand for the dielectric constant of the nanocomposite (PS-BTO), inclusion (BaTiO<sub>3</sub>) and matrix (PS), respectively. In this study, the dielectric constant of PS at room temperature was measured to be between 2.76 and 2.80 in the frequency range of 1 Hz to 1 MHz (as can be seen in Fig. 6, for 1 kHz). The measured effective dielectric constant of the PS-BTO nanocomposites and the calculated dielectric constant of BaTiO<sub>3</sub> nanoparticles in this frequency range are shown in Fig. 7. PS-BTO27 shows a higher and more stable effective dielectric constant than PS-BTO11. Using eqn (1), the dielectric constant of 27 nm BaTiO<sub>3</sub> nanoparticle (BTO27) decreases from 448 to 408 as the frequency

increases from 1 Hz to 1 MHz, whereas that of 11 nm nanoparticles (BTO11) is in the range from 349 at 1 Hz to 264 when the frequency reaches 1 MHz. Combined with the X-ray diffraction structural analysis results, the dielectric data suggest that the critical size for PS-capped BaTiO<sub>3</sub> nanoparticles is below but close to 11 nm.

## 4. Conclusions

PS-capped BaTiO<sub>3</sub> (PS-BTO) particles with sizes of 11 nm and 27 nm were prepared by a novel chemical route. Structural analysis demonstrates that the tetragonal phase is the dominant phase while the orthorhombic phase is also present in these nanoparticles at room temperature. The phase transitions in PS-BTO nanoparticles occur over broad temperature ranges, and a two phase coexistence is observed from 10 K to 428 K for PS-BTO11 and from 10 K to 408 K for PS-BTO27. As a consequence of the presence of multiple phases and the diluting polymer matrix, the anomalies of the dielectric properties associated with the structural phase transitions are broadened. With decreasing particle size, the BaTiO<sub>3</sub> shows less lattice distortion and lower dielectric constant at room temperature. These results indicate that the PS capping stabilizes the ferroelectric phases in BaTiO<sub>3</sub> and pushes the critical size to less than 11 nm. In addition, the BaTiO<sub>3</sub>–PS nanocomposites produced in the present study display an ultra-high dielectric permittivity, hence are promising for electrical capacitor applications.

## Acknowledgements

The Air Force Office of Scientific Research supported this research through grant FA9550-09-1-0388. The powder X-ray diffraction experiments and data analysis were performed at the Ames Laboratory, which is operated for the U.S. Department of Energy by Iowa State University under contract no. DE-AC02-07CH11358.

## References

- H. D. Megaw, *Ferroelectricity in Crystals*, Methuen, London, 1957.
- B. Jaffe, W. R. Cook and H. Jaffe, *Piezoelectric Ceramics*, Academic Press, New York, 1971, vol. 3.
- J. E. Spanier, A. M. Kolpak, J. J. Urban, I. Grinberg, L. Ouyang, W. S. Yun, A. M. Rappe and H. Park, *Nano Lett.*, 2006, **6**, 735–739.
- C. L. Wang and S. R. P. Smith, *J. Phys.: Condens. Matter*, 1995, **7**, 7163–7171.
- J. J. Urban, J. E. Spanier, O. Y. Lian, W. S. Yun and H. Park, *Adv. Mater.*, 2003, **15**, 423–426.
- M. H. Frey and D. A. Payne, *Phys. Rev. B: Condens. Matter Mater. Phys.*, 1996, **54**, 3158.
- K. Uchino, E. Sadanaga and T. Hirose, *J. Am. Ceram. Soc.*, 1989, **72**, 1555.
- S. Aoyagi, Y. Kuroiwa, A. Sawada, I. Yamashita and T. Atake, *J. Phys. Soc. Jpn.*, 2002, **71**, 1218–1221.
- Y. Fukui, S. Izumisawa, T. Atake, A. Hamano, T. Shirakami and H. Iwaka, *Ferroelectrics*, 1997, **203**, 227.
- Y. G. Wang, W. L. Zhong and P. L. Zhang, *Solid State Commun.*, 1994, **90**, 329.
- T. Hoshina, H. Kakemoto, T. Tsurumi, M. Yashima and S. Wada, *J. Appl. Phys.*, 2006, **99**, 054311.
- T. Hoshina, H. Kakemoto, T. Tsurumi, S. Wada, M. Yashima, K. Kato and M. Takata, *Key Eng. Mater.*, 2005, **301**, 239–242.
- T. Hoshina, H. Kakemoto, T. Tsurumi, S. Wada, M. Yashima, Y. Kuroiwa and S. Wada, *Key Eng. Mater.*, 2006, **320**, 131–134.

- 14 K. Ishikawa, K. Yoshikawa and N. Okada, *Phys. Rev. B: Condens. Matter Mater. Phys.*, 1988, **37**, 5852.
- 15 A. V. Polotai, A. V. Ragulya and C. A. Randall, *Ferroelectrics*, 2003, **288**, 93.
- 16 D. McCauley, R. E. Newnham and C. A. Randall, *J. Am. Ceram. Soc.*, 1998, **81**, 979.
- 17 M. R. Srinivasan, M. S. Multani, P. Ayyub and R. Vuayaraghavan, *Ferroelectrics*, 1983, **51**, 137.
- 18 A. J. Bell, A. J. Moulson and L. E. Cross, *Ferroelectrics*, 1984, **54**, 147.
- 19 K. Page, T. Proffen, M. Niederberger and S. Seshadri, *Chem. Mater.*, 2010, **22**, 4386–4391.
- 20 J. Li, J. Claude, L. E. Norena-Franco, S. Seok and Q. Wang, *Chem. Mater.*, 2008, **20**, 6304–6306.
- 21 J. Chon, S. Ye, K. J. Cha, S. C. Lee, Y. S. Koo, J. H. Jung and Y. K. Kwon, *Chem. Mater.*, 2010, **22**, 5445–5452.
- 22 P. K. Dutta, R. Asiaie, S. A. Akbar and W. Zhu, *Chem. Mater.*, 1994, **6**, 1542–1548.
- 23 L. Xie, X. Huang, C. Wu and P. Jiang, *J. Mater. Chem.*, 2011, **21**, 5897–5906.
- 24 M.-F. Lin, V. K. Thakur, E. J. Tan and P. S. Lee, *J. Mater. Chem.*, 2011, **21**, 16500–16504.
- 25 P. Kim, N. M. Doss, J. P. Tillotson, P. J. Hotchkiss, M. J. Pan, S. R. Marder, J. Y. Li, J. P. Calame and J. W. Perry, *ACS Nano*, 2009, **3**, 2581–2592.
- 26 H. M. Jung, J. H. Kang, S. Y. Yang, J. C. Won and Y. S. Kim, *Chem. Mater.*, 2010, **22**, 450–456.
- 27 X. Pang, L. Zhao, M. Akinc, J. K. Kim and Z. Lin, *Macromolecules*, 2011, **44**, 3746–3752.
- 28 A. P. Holm, V. K. Pecharsky, K. A. Gschneidner, R. Rink and M. N. Jirmanus, *Rev. Sci. Instrum.*, 2004, **75**, 1081.
- 29 B. Hunter, Rietica – A visual Rietveld program, International Union of Crystallography Commission on Powder Diffraction Newsletter No. 1998 Commission on Powder Diffraction Newsletter No. 20, (Summer, 1998) <http://www.rietica.org>.
- 30 A. C. Larson and R. B. Von Dreele, *General Structure Analysis System (GSAS)*, Los Alamos National Laboratory Report LAUR 86-748, Los Alamos, 2004.
- 31 K. Sakayori, Y. Matsui, H. Abe, E. Nakamura, M. Kenmoku, T. Hara, D. Ishikawa, A. Kokubu, K. Hirota and T. Ikeda, *Jpn. J. Appl. Phys.*, 1995, **34**, 5443.
- 32 P. Kim, S. C. Jones, P. J. Hotchkiss, J. N. Haddock, B. Kippelen, S. R. Marder and J. W. Perry, *Adv. Mater.*, 2007, **19**, 1001–1005.
- 33 S. Wada, T. Hoshina, H. Yasuno, M. Ohishi, H. Kakemoto, T. Tsurumi and M. Yashima, *Key Eng. Mater.*, 2006, **301**, 27–30.
- 34 J. C. Maxwell-Garnett, *Philos. Trans. R. Soc., A*, 1904, **203**, 385.
- 35 D. A. G. Bruggeman, *Ann. Phys.*, 1935, **24**, 636.
- 36 R. J. Landauer, *J. Appl. Phys.*, 1952, **23**, 779.